APPLICATION OF AN ADAPTIVE GRID PROCEDURE FOR THE CALCULATION OF TURBULENT SEPARATED FLOWS

F. MOUKALLED¹ and S. ACHARYA²†

¹Mechanical Engineering Department, American University of Beirut, Beirut, Lebanon ²Mechanical Engineering Department, Room 2513B CEBA, Louisiana State University, Baton Rouge, LA 70803, U.S.A.

(Received 18 December 1990; in revised form 4 September 1991)

Abstract—A solution-adaptive grid procedure is used to obtain solutions for turbulent flow over a backward-facing step, and comparisons are made with measurements. Comparisons between the solution-adaptive grid solution and the same-CPU-effort fixed grid solution demonstrates the superiority of solution-adaptive gridding over intuitive refinement of fixed grids. The relative importance of numerical errors compared with modeling errors is emphasized and it is shown that an assessment of modeling errors, without properly attempting to minimize numerical errors, can be very misleading. It is argued that solution-adaptive grid procedures provide a convenient vehicle for reducing numerical errors and should be used in calculations performed to evaluate physical models.

NOMENCLATURE

NOMENCEATURE	
$a_{\rm P}^{\phi}, a_{\rm E}^{\phi}, a_{\rm N}^{\phi}, a_{\rm N}^{\phi}, a_{\rm S}^{\phi}$ —Coefficients in the finite difference	t—Tangential coordinate
equation	u_i —Mean velocity in the x_i direction
A*—Constant in the law of the wall	u'_i —Velocity fluctuation in the x_i direction
b_{n0}^{ϕ} —Source term due to non-orthogonality	u_{in} —Inlet velocity
in the finite difference equation	$u_{\tau}^{u_{\tau}}$ —Friction velocity
b_0^{ϕ} —Source term in the finite difference	V^i —Adaptive grid solution at the <i>i</i> th refine-
equation	ment
b_p^{ϕ} —Source term due to the pressure gradi-	w—West face of a control volume
ent in the finite difference equation	W-West neighbor of the P grid point
$c_{\mu}, c_{\alpha}, c_{\beta}$ —Constants in equations (4)–(6)	W^{ϕ} —Weight function
C_1 —Skin friction coefficient	x_r —Reattachment length
e—East face of a control volume	x,—Cartesian coordinate
E-East neighbor of the P grid point	
f-Nonhomogeneous term in the conser-	Greek symbols
vation equation	α-Metric quantity
f ₁ —Constant for a given curve in the	$\alpha_1, \alpha_2, \alpha_3, \alpha_4$ —Constants
equidistribution law	β—Metric quantity
G—Rate of production of the turbulence	γ—Metric quantity
kinetic energy	δ_{ij} —Kronecker delta
G_1 , G_2 —Convective terms normal to the grid	ϵ —Turbulence dissipation rate
cell boundaries	η—Curvilinear coordinate
<i>J</i> —Jacobian	θ_1, θ_2 —Slopes of constant η and ξ curves
k—Turbulence kinetic energy	θ_3 —Angle of intersection, $(\theta_2 - \theta_1)$
L—Differential operator	κ —Constant in the law of the wall
l _t —Turbulence length scale	μ —Laminar viscosity
n-North face of a control volume; also	μ_t —Turbulent viscosity
normal coordinate	v _t —Eddy viscosity
N-North neighbor of the P grid point	ξ—Curvilinear coordinate
<i>p</i> —Pressure	π' —ith Level refined mesh
p'—Pressure fluctuation	ho—Density
P—Main grid point	σ_k —Effective Prandtl number for the turbulence
R—Local radius of curvature	kinetic energy
Re—Reynolds number	σ_c —Effective Prandtl number for the turbulence
s—South face of a control volume	dissipation rate
s_1 —Arc length along a line of constant η	τ_{ij} —Shear stress
s_2 —Arc length along a line of constant ζ	τ,Wall shear stress
S—South neighbor of the P grid point;	φ—Dependent variable
also step height	Γ ^φ —Diffusion coefficient
S^{ϕ} —Source term	$\Delta \xi$, $\Delta \eta$ —Cell boundary sizes in the ξ and η directions
	in the transformed plane

fluctuation in the x_i direction ocity velocity e grid solution at the ith refinece of a control volume eighbor of the P grid point function hment length n coordinate quantity ıts quantity quantity ker delta nce dissipation rate ear coordinate of constant η and ξ curves f intersection, $(\theta_2 - \theta_1)$ it in the law of the wall r viscositv nt viscosity scosity ear coordinate el refined mesh

Λ—Control function

 Φ , Φ_1 —Weight function

[†]To whom all correspondence should be addressed.

 Ψ , Ψ_1 —Weight function Ω —Control function

Subscripts

e, w, n, s—Refer to control volume faces P, E, W, N, S—Refer to grid points

x, y, η, ξ—Indicate differentiation with respect to x, y, η and ξ max—Maximum value min—Minimum value n—Normalized value t—Refers to turbulent flow

INTRODUCTION

Model improvements for turbulent separated flows are based on an assessment of existing models by comparing predictions with corresponding measurements. The differences between predictions and measurements represent the cumulative effect of both numerical errors and modeling errors. However, frequently the importance of numerical errors are ignored, and the differences between predictions and measurements are attributed entirely to modeling errors. Clearly, model improvements, based on such an assessment of modeling errors, are likely to be misleading. One objective of this paper is to apply a solution-adaptive grid calculation procedure for the turbulent separated flow past a backward-facing step, and to demonstrate through comparisons with measurements and fixed grid solutions, the relative importance of numerical errors in making an assessment of modeling errors.

It could be argued that instead of using a solution-adaptive grid procedure, the conventional fixed grid could simply be refined intuitively. However, as will be seen, for the same CPU-effort the solution-adaptive grid procedure is superior to the fixed grid procedure.

Attention is focused in this paper on the widely used $k-\epsilon$ model [1, 2] which has been applied to many separating flows [3-8]. The observed weaknesses and poor predictions of the standard $k-\epsilon$ model for flows with recirculation, streamline curvature and buoyancy effects, have led to the development of several refined $k-\epsilon$ models [9–15]. Jones and Launder [9] proposed a low-Reynolds number version of the $k-\epsilon$ model with which the calculations can be extended to the near-vicinity of the wall. Chieng and Launder [8] studied pipe expansion geometry by using both the standard and the low-Reynolds number $k-\epsilon$ models along with a near-wall procedure which was later extended by Amano [10]. Gooray et al. [11] combined these models and developed a two-pass procedure, with a high-Reynolds number model applied upstream of reattachment and a low-Reynolds number model used downstream of reattachment. The standard high-Reynolds model accounted for streamline curvature effects in the recirculation region. Improvements to the above models, in which pressure strain effects and wall damping corrections are included, were subsequently developed by Gooray and co-workers [12, 13]. Leschziner and Rodi [14] derived functional relations for some of the constant coefficients employed in the $k-\epsilon$ model through the use of algebraic stress closure relations. These improvements sensitize the turbulence model to the effects of streamline curvature. Nagano and Kim [15] proposed an improved form of the $k-\epsilon$ model in which assumptions for the turbulent Prandtl number are not required.

None of the above models, however, resolved all the issues. In assessing model performance, predictions and measurements were compared. However, as noted earlier, predictions are subject to numerical inaccuracies, so it is not the turbulence model alone which is responsible for the lack of agreement with experimental data—in addition, numerical errors play an important role. These numerical errors are due to the discretization errors (that arise from differencing approximations) and the round-off errors (machine dependent).

The discretization errors are proportional to the product of the local grid spacing raised to some power and a measure of the local solution variation. Thus, these errors can be reduced by decreasing the local mesh size. Reducing the mesh size over the entire domain increases the computational cost dramatically and therefore, the grid points should be concentrated in the important regions of the physical domain to economically reduce the discretization errors. Prior to the solution, however, these important regions are not known, and a dynamic procedure in which the grid points move in accordance with the evolving solution is necessary. Such methods, called solution-adaptive grid methods, were proposed by many workers [16–26]. In this paper, the solution-adaptive grid procedure developed by Acharya and Moukalled [25, 26] and characterized by Local Adaptation with Multigridding and Equidistribution concepts (LAME) is adopted. Unlike other related studies, the LAME procedure [25, 26] permits the flagging of an arbitrarily shaped region in the computational domain, and further, instead of refining the flagged region

uniformly as in most other studies, performs the refinement using an error equidistribution method. It should also be pointed out that, in general, in demonstrating the utility of solution-adaptive grid procedures, simple laminar flow problems are solved and reported in the literature. In this paper the LAME solution-adaptive grid procedure is applied to a more complex turbulent flow problem.

One last issue that should be addressed here is related to flow field calculations, in which the possibility of predicting checkerboard pressure and velocity fields is usually avoided through the use of a staggered grid for the velocity components. Adaptation on such a grid implies redefining three different sets of grid points at each step. This can be very expensive and is avoided here by using the calculation procedure on a non-staggered curvilinear grid developed by Acharya and Moukalled [27].

To reiterate the main motive of this paper numerical errors and modeling errors occur together in turbulent flows, and no conclusions related to the performance of turbulence models can be drawn without properly assessing numerical errors. This clearly represents a serious obstacle to the development and testing of these models. One objective of this paper, as noted earlier, is to predict the turbulent flow characteristics behind a backward-facing step using a solution-adaptive grid procedure [25, 26] and to demonstrate the relative importance of the numerical errors vs modeling errors. By comparing the solution-adaptive grid calculation with the same-CPU-effort fixed grid calculation, it is the intent of this paper to demonstrate the superiority of solution-adaptive grid procedures over same-CPU-effort fixed grid procedures and to argue that in assessing modeling errors, for the same CPU-effort, the more accurate, solution-adaptive grid procedure should be used. It is not the intent of this paper to present grid-independent results or definitively assess modeling errors with the two-equation turbulence models. A secondary objective of the paper is the application of the solution-adaptive grid procedure to the more commonly encountered turbulent flow problem of flow over a backward-facing step, since most reported studies have applied the adaptive grid procedure only to simple laminar flows.

BASIC CONSERVATION EQUATIONS

The mean transport equations governing the situation under consideration (written in tensor notation) are given by

Continuity:
$$\partial(\rho u_i)/\partial x_i = 0 \tag{1}$$

and

Momentum:
$$\partial (\rho u_i u_i)/\partial x_i = -\partial p/\partial x_i + \partial \tau_{ii}/\partial x_i,$$
 (2)

where

$$\tau_{ij} = \mu(\partial u_i/\partial x_j + \partial u_j/\partial x_i) - \frac{2}{3}\mu(\partial u_k/\partial x_k)\delta_{ij} - \overline{\rho u_i' u_j'}.$$
 (3)

In the above equations, u_i' and u_i are the fluctuating and mean velocity components in the x_i direction, δ_{ij} is the Kronecker delta, ρ is the fluid density, μ is the fluid viscosity and τ_{ij} is the Newtonian viscous stress plus the Reynolds stress $(-\overline{\rho u_i' u_j'})$. The unknown Reynolds stresses have to be modeled, which leads to the well-known closure problem. This task is accomplished through the use of turbulence models.

In the following section the standard $k-\epsilon$ model [2] and a modified version [14] that is used in this paper are reviewed briefly. Then the numerical techniques used to solve the resulting system of partial differential equations are described. These include the calculation procedure on a non-staggered curvilinear grid [27] and the LAME solution-adaptive grid methodology [25, 26].

THE TURBULENCE MODELS

The standard $k-\epsilon$ model [2] utilizes the eddy viscosity/diffusivity concept and relates the eddy viscosity v_t to the turbulence kinetic energy k (where $k = \frac{1}{2} \overline{u_i' u_i'}$) and turbulence dissipation rate ϵ ($\epsilon \sim k^{3/2}/l_t$, where l_t is a turbulence length scale) via the Kolmogorov-Prandtl relation:

$$-\overline{u_i'u_j'} = v_t[\partial u_i/\partial x_j + \partial u_j/\partial x_i] - \frac{2}{3}k\delta_{ij}, \quad v_t = c_\mu k^2/\epsilon.$$
 (4)

The distribution of k and ϵ are determined from the following modeled transport equations:

$$u_i \partial k / \partial x_i = \partial \left[(v_i / \sigma_k) (\partial k / \partial x_i) \right] / \partial x_i + G - \epsilon \tag{5}$$

and

$$u_i \partial \epsilon / \partial x_i = \partial [(v_t / \sigma_\epsilon) (\partial \epsilon / \partial x_i)] / \partial x_i + c_{\epsilon_i} (\epsilon / k) G - c_{\epsilon_i} (\epsilon^2 / k). \tag{6}$$

Equations (5) and (6) are derived from the Navier-Stokes equations and describe how the rate of change of k and ϵ are balanced by convective and diffusive transport and by the production and molecular dissipation processes.

The $k-\epsilon$ model contains the five empirical constants c_{μ} , σ_{k} , σ_{ϵ} , $c_{\epsilon_{1}}$ and $c_{\epsilon_{2}}$. The commonly accepted values for these constants are 0.09, 1, 1.3, 1.45 and 1.9, respectively. The standard model presented so far is applicable only to flows or flow regions with high turbulence Reynolds number, $\text{Re}_{t} = v_{t}/v$, and cannot be applied near walls, where viscous effects become dominant. This problem can be overcome by either of the following two approaches. First, the low turbulence Reynolds number model suggested by Jones and Launder [9] can be used with a sufficient number of grid points in the viscous sublayer region. However, this practice is rather expensive computationally. The second alternative, used in the present work, is based on the assumption that the near-wall turbulent flow resembles a Couette flow, and the universal law of the wall equations are valid. With these assumptions, the resultant velocity parallel to the wall, u_{p} , the kinetic energy, k_{p} , and the dissipation rate, ϵ_{p} , at a distance y_{p} from the wall are related to the friction velocity u_{τ} ($u_{\tau} = \sqrt{\tau_{w}/\rho}$, where τ_{w} is the wall shear stress) by the following relations:

$$u_p/u_\tau = (1/\kappa)\ln(\mathbf{A}^* u_\tau y_p/v), \quad k_p = u_\tau^2/\sqrt{c_\mu}, \quad \epsilon_p = u_\tau^3/(\kappa y_p). \tag{7}$$

In the above equation, κ and A* are the constants from the law of the wall with values of 0.4 and 9, respectively.

The above standard form of the k- ϵ model does not account for important secondary strain effects, such as those resulting from curvature. Therefore, modifications accounting for the effects of streamline curvature should be introduced into the original model in cases where these effects are important. Such modifications are described in the following subsection.

Modified version

Numerical predictions of turbulent separated flows using the standard $k-\epsilon$ model described above, are found to be in less-than-satisfactory agreement with experimental data. In particular, the dimension of the recirculation region, which depends on the diffusive transport in the bordering shear layer, is underpredicted. Experimental data show a high sensitivity to curvature of the turbulent shear stress and of the degree of anisotropy between the normal stresses. Since the $k-\epsilon$ model can recognize only the explicit extra terms due to curvature in the mean motion and turbulent transport equations, it will underpredict the curvature effects, and has to be suitably modified. This is in contrast to the algebraic stress and Reynolds stress models which need no such modification. Several modified $k-\epsilon$ models have been developed to incorporate the streamline curvature caused by the surface curvature as well as by swirl or rotation. Many of these models employ a modification of the length scale, while others incorporate this effect through the modification of c_{μ} needed in the evaluation of the eddy viscosity. One such modification, adopted for the present calculation, is due to Leschziner and Rodi [14] and is based on a simplification of the algebraic Reynolds stress model. The modification is to use a functional relation for c_{μ} instead of using the constant value of 0.09. With this modification, c_{μ} is calculated as follows:

$$c_{u} = 0.09/[1 + 0.57(k/\epsilon)^{2}(\partial u_{t}/\partial n + u_{t}/R)(u_{t}/R)].$$
 (8)

In the above equation, R is the local radius of curvature, u_t is the tangential velocity, and n and t are the streamline coordinates shown in Fig. 1. Details can be found in Ref. [14].

With this modification, the turbulence model is sensitized to curvature effects and, therefore, the use of this modified version is expected to improve the numerical predictions by decreasing the physical error. The largest improvement in the results is expected to be accomplished when using the modified $k-\epsilon$ model in conjunction with the LAME solution-adaptive grid procedure, in which case, both the physical and numerical errors are reduced.

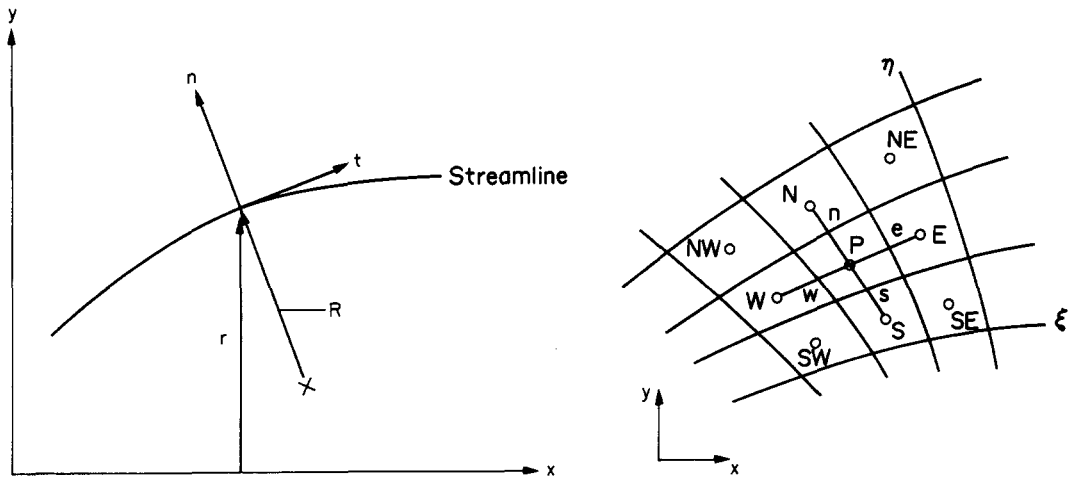


Fig. 1. Streamline coordinate system.

Fig. 2. Finite difference grid representation.

CALCULATION ON A NON-STAGGERED CURVILINEAR GRID

When solving the flow equations (conservation of mass and momentum) using SIMPLE(Semi Implicit Method for Pressure Linked Equations)-type algorithms [28], a staggered grid arrangement is generally adopted to avoid checkerboard pressure and velocity fields. Therefore, three sets of mesh positions (one for each of the two components of velocity and the third for pressure) and associated metric quantities have to be calculated and stored. If grid adaptation is performed, the grid changes at every step and therefore three sets of grid positions and metric quantities have to be calculated at each step. To avoid this cumbersome and computationally expensive procedure, a non-staggered grid arrangement is desirable, but the solution algorithm must be suitably modified to avoid checkerboard pressure and velocity fields. Such modifications have been reported by Acharya and Moukalled [27], Hsu [29], Reggio and Camarero [30], Rhie and Chow [31] and Abdallah [32].

In this paper, the SIMPLEM (SIMPLE—Modified) algorithm proposed by Acharya and Moukalled [27] is used. This algorithm has been compared with some of the other algorithms and has been shown to have superior characteristics [27]. In the discussion below, the various steps of the calculation process, including grid generation, discretization of the conservation equations and the SIMPLEM solution algorithm, are described briefly. Additional details are found elsewhere [33].

Grid generation

A curvilinear grid is generated in an arbitrary shaped region by solving the following elliptic system of equations [34]:

$$\alpha x_{\xi\xi} - 2\beta x_{\xi\eta} + \gamma x_{\eta\eta} = -J^2(x_{\xi}\Lambda + x_{\eta}\Omega) \tag{9}$$

and

$$\alpha y_{\xi\xi} - 2\beta y_{\xi\eta} + \gamma y_{\eta\eta} = -J^2(y_{\xi}\Lambda + y_{\eta}\Omega), \tag{10}$$

where $\xi(x, y)$ and $\eta(x, y)$ are the curvilinear coordinates, x and y are the cartesian coordinates, α , β , γ and J are metric quantities, given by

$$\alpha = x_n^2 + y_n^2, \quad \beta = x_{\varepsilon} x_n + y_{\varepsilon} y_n, \quad \gamma = x_{\varepsilon}^2 + y_{\varepsilon}^2, \quad J = x_{\varepsilon} y_n - x_n y_{\varepsilon}, \tag{11}$$

and Λ and Ω are control functions that can be chosen to provide denser clustering in certain specified areas.

For adaptive grid generation, the ideas of Anderson and Steinbrenner [35] are used. In Ref. [35], equations (9) and (10) are recast into error equidistribution laws by relating Λ and Ω to the local error estimate or weighting function. For this, the relationship between the weighting functions W^{ϕ}

and the control functions Λ and Ω in equations (9) and (10) are easily derived by considering the equidistribution law along a constant- η line, i.e.

$$(s_1)_{\xi} W^{\phi} = f_1(\eta), \tag{12}$$

where s_1 is the arc length along a line of constant η , $f_1(\eta)$ is a constant for a given curve and W^{ϕ} is the weighting function. Differentiating equation (12) with respect to ξ , the following equation is obtained:

$$(s_1)_{\xi\xi} + [(W^{\phi})_{\xi}/W^{\phi}](s_1)_{\xi} = 0. \tag{13}$$

Returning to equations (9) and (10), and defining $\Phi = J^2 \Lambda / \alpha$ and $\psi = J^2 \Omega / \gamma$ and then eliminating ψ between the two equations, an equation having s_1 as the dependent variable is obtained, i.e.

$$(s_1)_{\xi\xi} + \Phi_1(s_1)_{\xi} = 0,$$
 (14)

where

$$\Phi_1 = \Phi - [(\theta_1)_{\xi} - 2(\theta_2)_{\xi}] \cot \theta_3 - (s_1)_{\xi} (\theta_2)_{\eta} \sin \theta_3 / (s_2)_{\xi}. \tag{15}$$

In the above equation θ_1 and θ_2 are the slopes of constant- η and constant- ξ curves, θ_3 is the angle of intersection and s_2 is the arc length along a line of constant ξ . A similar equation can be derived along a line of constant ξ .

Comparison of equations (13) and (14) leads to

$$\Phi_1 = (W^{\phi})_{\varepsilon} / W^{\phi} \tag{16}$$

and, similarly,

$$\Psi_1 = (W^{\phi})_{\alpha}/W^{\phi}. \tag{17}$$

Thus, the elliptic grid generation procedure [34] can be interpreted as an equidistribution law if the control functions Φ_1 and Ψ_1 are obtained from equations (16) and (17). This is the procedure adopted in this paper for performing grid adaptation during the calculation.

Discretization of the conservation equations

The conservation equations (1), (2), (5) and (6) can be represented using the following standard equation, written in curvilinear coordinates in terms of a general scalar property ϕ :

$$\{\rho G_1 \phi - (\Gamma^{\phi}/J)(\alpha \phi_{\varepsilon} - \beta \phi_n)\}_{\varepsilon} + \{\rho G_2 \phi - (\Gamma^{\phi}/J)(\gamma \phi_n - \beta \phi_{\varepsilon})\}_n = S^{\phi}J, \tag{18}$$

where S^{ϕ} is the source term, G_1/J and G_2/J are the contravariant velocity components, with G_1 and G_2 defined by

$$G_1 = u y_n - v x_n, \quad G_2 = v x_{\varepsilon} - u y_{\varepsilon}, \tag{19}$$

and ρ and Γ^{ϕ} denote, respectively, the fluid density and the diffusion coefficient. The control volume approach is adopted here. With this approach the domain is subdivided into a number of control volumes, each associated with a grid point. The finite difference form is obtained by integrating equation (18) over the control volume shown in Fig. 2. This leads to an integral balance equation of the form

$$[\rho G_1 \phi - (\Gamma^{\phi}/J)(\alpha \phi_{\xi} - \beta \phi_{\eta})]_{e} \Delta \eta - [\rho G_1 \phi - (\Gamma^{\phi}/J)(\alpha \phi_{\xi} - \beta \phi_{\eta})]_{w} \Delta \eta + [\rho G_2 \phi - (\Gamma^{\phi}/J)(\gamma \phi_{\eta} - \beta \phi_{\xi})]_{o} \Delta \xi - [\rho G_2 \phi - (\Gamma^{\phi}/J)(\gamma \phi_{\eta} - \beta \phi_{\xi})]_{s} \Delta \xi = S_{p}^{\phi} J \Delta \xi \Delta \eta.$$
 (20)

In the above equation, ϕ , ϕ_{ξ} and ϕ_{η} at the east, west, north and south faces are expressed in terms of the grid point (P) value by using the power law scheme [28]. The resulting discretization equation can be written as

$$a_{\rm P}^{\phi}\phi_{\rm P} = a_{\rm E}^{\phi}\phi_{\rm E} + a_{\rm W}^{\phi}\phi_{\rm W} + a_{\rm N}^{\phi}\phi_{\rm N} + a_{\rm S}^{\phi}\phi_{\rm S} + b_{\rm 0}^{\phi} + b_{\rm n0}^{\phi} + b_{\rm p}^{\phi}, \tag{21}$$

where a_P^{ϕ} , a_E^{ϕ} , a_N^{ϕ} , a_N^{ϕ} and a_S^{ϕ} are the convection-diffusion coefficients, b_p^{ϕ} is the source term contribution, b_{n0}^{ϕ} is the contribution due to non-orthogonality and b_p^{ϕ} is the pressure gradient contribution, which has a non-zero value if ϕ represents the two velocity components. The expressions for these coefficients can be found in Ref. [33].

An equation for the remaining unknown pressure is established by combining the continuity and momentum equations. This is done by rewriting equation (21) with ϕ replaced by u and v, dividing across by a_p^u and a_p^v , respectively, and defining pseudo-velocities \hat{u}_p and \hat{v}_p as

$$\hat{u}_{P} = \left(\sum_{n = E, W, N, S} a_{n}^{u} u_{n} + b_{0}^{u} + b_{n0}^{u} \right) / a_{P}^{u}$$
(22)

and

$$\hat{v}_{P} = \left(\sum_{n = E, W, N, S} a_{n}^{v} v_{n} + b_{0}^{v} + b_{n0}^{v}\right) / a_{P}^{v}.$$
(23)

The momentum equations can then be written as

$$u_{\rm P} = \hat{u}_{\rm P} + (B^{u}p_{\rm F} + C^{u}p_{\rm n})_{\rm P} \tag{24}$$

and

$$v_{\rm p} = \hat{v}_{\rm p} + (B^{\rm v}p_{\rm g} + C^{\rm v}p_{\rm n})_{\rm p}. \tag{25}$$

Introducing equations (22) and (23) into the definitions of the contravariant terms G_1 and G_2 given by equation (19), the following equations are obtained:

$$G_1 = \hat{G}_1 + (B^u y_n - B^v x_n) p_{\xi} + (C^u y_n - C^v x_n) p_{\eta}$$
(26)

and

$$G_{2} = \hat{G}_{2} + (C^{v}x_{\varepsilon} - C^{u}y_{\varepsilon})p_{u} + (B^{v}x_{\varepsilon} - B^{u}y_{\varepsilon})p_{\varepsilon}, \tag{27}$$

where \hat{G}_1 and \hat{G}_2 are based on \hat{u} and \hat{v} as defined by equations (22) and (23), respectively. Upon introducing G_1 and G_2 , given by equations (26) and (27), into the continuity equation given by

$$(\rho G_1 \Delta \eta)_{\rm e} - (\rho G_1 \Delta \eta)_{\rm w} + (\rho G_2 \Delta \xi)_{\rm n} - (\rho G_2 \Delta \xi)_{\rm s} = 0, \tag{28}$$

the finite difference form of the pressure equation is obtained and can be written as

$$a_{p}p_{p} = \sum_{n \in F, W, N, S} a_{n}^{p}p_{n} + b_{0}^{p} + b_{n0}^{p},$$
(29)

where b_0^p has an expression given by the negative of the left-hand side of equation (28) with the G's replaced by \hat{G} 's.

The numerical solution to the flow problem is then obtained by solving a system of algebraic equations similar to equation (21) or (29) along with the appropriate boundary conditions.

Solution algorithm

The sequence of operations in the SIMPLEM algorithm on a fixed grid is as follows:

- 1. Start with guessed fields u^* , v^* and p^* .
- 2. Calculate the coefficients of the momentum equations and then \hat{u} and \hat{v} . Use these values to find \hat{G}_1 and \hat{G}_2 at the grid nodes. Interpolate linearly to find \hat{G}_1 and \hat{G}_2 at the control volume faces.
- Calculate the coefficients of the pressure equation and solve it to obtain a new pressure field.
- 4. Use this new pressure field to calculate the pressure gradients in the momentum equations using a $2 \Delta \xi$ or $2 \Delta \eta$ centered difference scheme.
- 5. Update G_1^* and G_2^* at the interfaces [equations (26) and (27)] using the new pressure field and using a $1 \Delta \xi$ or $1 \Delta \eta$ centered difference scheme for ∇p .
- 6. Based on the new G_1 and G_2 recalculate the coefficients of the momentum equations and solve them to obtain new velocity fields u^* and v^* .
- 7. Solve for all other scalar variables.
- 8. Return to Step 2 with the new values of u^* and v^* and repeat until a converged solution is obtained.

THE LAME SOLUTION-ADAPTIVE GRID PROCEDURE

In the LAME solution-adaptive grid procedure [25, 26], the grid is refined locally in flagged regions where the error estimate exceeds a specified threshold value. Compared with other adaptive grid techniques, the LAME procedure has the advantage that the flagged region in the computational space, where the preliminary calculations are being performed, can be arbitrarily shaped. More importantly, grid refinement in each flagged region is not done uniformly, as in other studies, but by an equidistribution law that clusters the points more densely in regions of higher error estimates within the flagged region. The solutions at different grid levels are successively improved using a multi-grid method. In the discussion that follows, the local grid refinement procedure using an error equidistribution law is described first followed by a description of the multi-grid calculation procedure.

Local grid refinement using an error equidistribution law

The solution process is initiated by generating a relatively coarse mesh in the domain by solving the set of Poisson equations [equations (9) and (10)]. After a preassigned number of iterations, an error estimate or weighting function is calculated at each grid point. For this purpose, a weighting function W^{ϕ} , for each dependent variable ϕ is defined as

$$W^{\phi} = \alpha_1 J |\nabla^2 \phi| + \alpha_2 |\nabla \phi|^2 + \alpha_3 J |\nabla \xi \cdot \nabla \eta| + \alpha_4 J (\nabla \xi^2 + \nabla \eta^2), \tag{30}$$

where α_1 , α_2 , α_3 and α_4 are constants. The first two terms represent a measure of the truncation error, while the last two terms represent grid orthogonality and smoothness and can be viewed as a measure of the geometric error due to grid distortion. To flag points, a normalized weighting function W_p^{ϕ} is defined as

$$W_{\rm n}^{\phi} = (1 + W^{\phi})/(1 + W_{\rm max}^{\phi}) \tag{31}$$

and points are flagged if the normalized weighting function is greater than a preassigned value (generally in the range of 0.4–0.6). A flagged region is identified as a cluster of contiguous flagged points. There can be more than one cluster, and each cluster in the $\xi-\eta$ space can have an arbitrary shape. In each flagged region, the grid is refined using an error equidistribution method. The adaptive grid generation starts by assigning ξ_{\min} , ξ_{\max} , η_{\min} and η_{\max} for each flagged region. Once this is done, the number of grid points along each boundary is doubled and a preliminary grid is generated in the flagged region. The values of Λ and Ω , which are related to the weighting functions or error measures W^{ϕ} through equations (16) and (17), are interpolated on this preliminary grid from the corresponding coarse grid values and equations (9) and (10) are solved to obtain the equidistributed mesh in the flagged region. This mesh, is used as a new guess, Λ and Ω are interpolated on to the new positions, and the above process is repeated until the grid points undergo no further change in position. The resulting grid is non-uniform with a finer mesh in the regions where the weighting function values are higher. After obtaining the interior grid distribution, the boundary points are adjusted, if possible, so that the grid is orthogonal to the boundary.

The above procedure for generating an equidistributed grid is repeated in each flagged region. Once the equidistributed mesh in each flagged region is obtained, the next step of obtaining the solution in each of these regions is initiated.

Boundary conditions for the locally refined regions

In order to obtain a solution in the flagged region, boundary conditions have to be interpolated from the coarse grid solution along the boundaries of the flagged region. The values at the corner of the coarse grid control volume faces along the boundaries of the flagged region are first determined as the weighted average of the four neighboring coarse grid points. Linear interpolation is then used between the coarse grid corner values to calculate the values at the fine grid points along the boundary of the flagged region. For flow problems, a conservative interpolation procedure is used in calculating the interpolated mass flow rates, needed in the pressure equation, across the zonal boundaries.

Multi-grid calculations

The solution accuracy in the flagged region depends on the accuracy of the outer grid solution. To improve the solution accuracy on the outer mesh, a multi-grid type approach is used. In this approach, the solution V^0 in the outer grid π^0 is obtained first, and the outer grid solution is prolongated to the embedded refined grid π^1 by interpolating the boundary conditions for the refined grid from the outer grid solution and then obtaining the refined grid solution V^1 . The refined grid solution is prolongated to the next level of the refined mesh π^2 . This process is continued to the finest refinement level π^n . Once the solution in the finest mesh has been obtained, the solution process steps back to its outer mesh π^{n-1} and recalculates the solution with restriction or correction terms added to the outer grid equations in the fine grid region π^n . These correction terms are such that the resulting corrected solution V^{n-1} is equal to V^n in the overlap region π^n . This process is continued till the outermost grid π^0 is reached. This completes one prolongation sweep and one restriction sweep. The second prolongation sweep is then initiated, and at any refinement level i, since the outer solution V^{i-1} is more accurate in view of the correction terms added in the previous restriction sweep, the boundary conditions interpolated along the boundaries of π^i from V^{i-1} will be more accurate and therefore the solution V^i will be better than the solution in the previous prolongation sweep. These sweeps can be continued to the desired levels of accuracy.

The coarse to fine grid information transfer in the prolongation operation has already been described in the previous section and consists of a suitable method for interpolating the boundary conditions along the boundaries of the flagged region and obtaining a fine grid solution in the flagged region. Attention is now turned to the restriction or correction operation that applies the fine grid solution V^i to the coarse grid equations in π^i such that the resulting outer grid solution V^{i-1} in π^i is equal to V^i .

If ϕ is any dependent variable, then the conservation equations on both the coarse (π^{i-1}) and fine (π^i) grid regions cast in operator forms are

$$L^{i-1}\phi^{i-1} = f^{i-1} \text{ in } \pi^{i-1}$$
(32)

and

$$L^i \phi^i = f^i \text{ in } \pi^i, \tag{33}$$

where the superscript i-1 identifies the outer or coarse grid terms, the superscript i denotes the fine grid terms and L is the differential operator. The expressions for L for the pressure p and for a general dependent variable ϕ are as follows:

$$L_{p} = (B^{u}y_{\eta} - B^{v}x_{\eta})p_{\xi} + (C^{u}y_{\eta} - C^{v}x_{\eta})p_{\eta} + (C^{v}x_{\xi} - C^{u}y_{\xi})p_{\eta} + (B^{v}x_{\xi} - B^{u}y_{\xi})p_{\xi}$$
(34)

and

$$L_{\phi} = \{ \rho G_1 \phi - (\Gamma^{\phi}/J) (\alpha \phi_{\mathcal{E}} - \beta \phi_n) \}_{\mathcal{E}} + \{ \rho G_2 \phi - (\Gamma^{\phi}/J) (\gamma \phi_n - \beta \phi_{\mathcal{E}}) \}_n. \tag{35}$$

In the restriction operation, it is desirable that the outer coarse grid solutions in the fine grid overlap region should equal the computed fine grid values, which are more accurate. This can be done by setting

$$L^{i-1}\phi^{i-1} = L^{i-1}\phi^i \quad \text{in } \pi^i \tag{36}$$

and

$$L^{i-1}\phi^{i-1} = f^{i-1} \quad \text{in } (\pi^{i-1} - \pi^i). \tag{37}$$

The expression on the right-hand side of equation (36) is the coarse grid correction term representing the restriction operation. By solving this system of equations, the values of the dependent variable on the coarse grid inside the refined region are exactly equal to the values obtained from the solution on the fine grid. This, in turn, causes the coarse grid solution in the non-refined parts of the domain to improve as the iterations progress.

RESULTS AND DISCUSSION

Results are presented using both the conventional and the adaptive grid techniques, with the intent of studying the numerical and physical errors associated with the numerical solution of turbulent separated flows. As previously stated, two turbulence models are employed; the standard $k-\epsilon$ model and a modified version of the model suggested by Leschziner and Rodi [14]. Three grid sizes are utilized in obtaining the results: a relatively coarse 20×8 grid; a finer 34×16 grid; and a reasonably fine 50×35 grid. The 34×16 fixed grid takes about the same CPU-effort as the 20×8 adaptive grid and the 50×35 fixed grid takes the same CPU-effort as the 34×16 adaptive grid; thus, a comparison of the results of the conventional and the adaptive grid methods for the same level of computational effort can be made. The adaptive grid solution is started either on the 20×8 grid or on the 34×16 grid and then refinement is done automatically where needed. The 34×16 fixed mesh contains 544 grid points, the 34×16 adapted mesh contains 1088 total grid points (note that the mesh is refined in critical regions, thus adding more points) and the 50×35 mesh uses 1750 grid points. In the literature for the flow past back steps or past ribs, numerical results have been reported using, for example, 450 points [36], 700 points [4, 12, 13] and 1406 points [14]. The number of points used in the present calculations are therefore typical of those used in the literature.

In this paper, one level of refinement is performed and all numerical results are compared with the available experimental data. The values of α_1 and α_2 in the definition of weighting function [equation (30)] have been assigned to be 1, while α_3 and α_4 have been set to zero.

The separated flow problem chosen is that of flow over a backward-facing step, which has received a great deal of attention in the literature [3, 4, 37–39]. In this paper the physical situation shown in Fig. 3, and studied experimentally by Chandrasuda and Bradshaw [38], is considered. Figure 3 represents the vertical centerplane of a wind tunnel, 127 mm high, with a backward-facing step of height S = 51 mm. The tunnel roof slopes downwards at a small angle of 1.7° downstream of the step to simulate a streamline in an infinitely high tunnel. The computations in the streamwise direction are extended up to 16S, where the streamwise gradients in the flow can be assumed to be small. The inlet velocity $u_{\rm in}$, assumed uniform, is 31.5 m/s. This velocity gives a Reynolds number based on the step height of about 10^{5} . The governing equations for the flow were given in previous sections. The turbulence intensity of the inlet stream is assumed to be 1% of the total mean kinetic energy, and the dissipation rate ($c = c_{\mu}k^{2}/v_{\tau}$) is taken to be 10% of the square of the turbulence kinetic energy. At the walls, the law of the wall, as explained previously, is used. At the flow exit, the gradients of all variables are assumed to be zero.

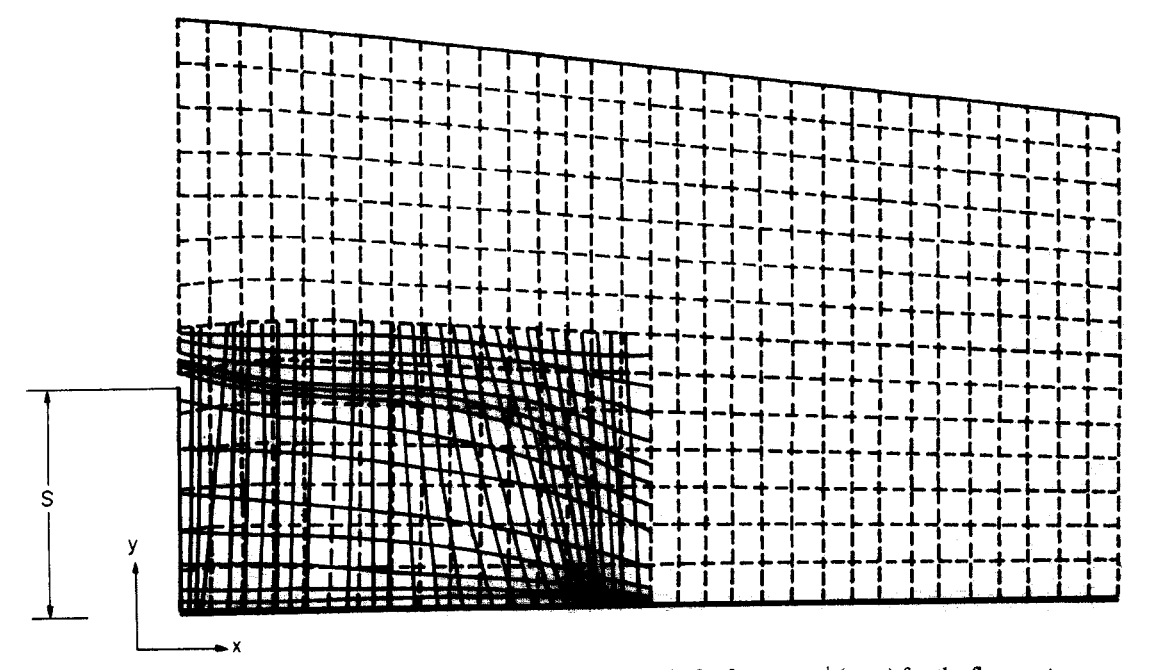


Fig. 3. Initial mesh π^0 (---) and adapted mesh after one level of refinement π^1 (----) for the flow past a step.

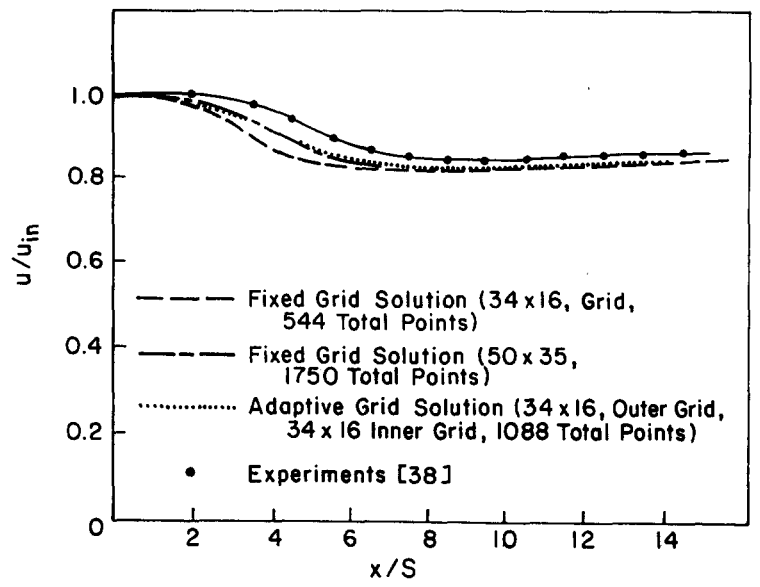


Fig. 4. Streamwise u-velocity profile at y/S = 1.8 (standard turbulence model).

Mean velocities were measured in Ref. [38] with either a plane-ended circular pilot tube or a hot-wire anemometer. In reverse-flow regions, the hot-wire data is unreliable, and the measured data should therefore be treated with caution below the dividing streamline. Turbulence is measured using the hot-wire anemometer, but again, due to the uncertainty in the reverse-flow regions, Chandrasuda and Bradshaw [38] present turbulence intensity results only in the regions of positive mean flow.

Figure 3 also shows the 34×16 outer grid (---) and the adapted 34×16 inner grid (---) in the flagged region. The flagged region is based on the error estimates for the *u*-velocity and the error estimates for the turbulence kinetic energy. In order to have a more orthogonal system, the flagged region needing refinement is enlarged slightly.

Representative results obtained with the $k-\epsilon$ model and its modified version are shown in Figs 4-13. In Figs 4-8 the standard $k-\epsilon$ model results are presented using both the conventional fixed grid (34 × 16 and 50 × 35 grids) and the present adaptive grid (34 × 16 outer grid and 34 × 16 inner grid) techniques. The corresponding modified $k-\epsilon$ model prediction are shown in Figs 9-13. For purposes of comparison the 20 × 8 adaptive grid solution has also been included in Figs 9-13.

The streamwise mean u-velocity component at y/S = 1.8 is plotted in Fig. 4 as a function of x/S. The improvement in the predictions after adaptation on the 34×16 grid can be seen easily. Note that this comparison is in the free stream region where the grid is not flagged, and the improvements in the adaptive grid solution are due to the multi-grid strategy adopted. The adaptive grid solution in this region is more or less identical to the same-CPU-effort 50×35 fixed grid calculation, but is much better than the 34×16 fixed grid solution. The velocity at y/S = 1.8 decreases until reattachment, then increases very slowly. This increase is attributed to the decrease in the cross-sectional area of the tunnel.

The skin friction coefficient, C_f , is defined as

$$C_{\rm f} = \tau_{\rm w}/[\frac{1}{2}\rho u_{\rm in}^2],$$
 (38)

where τ_w is the shear stress along the bottom wall. The predicted values (Fig. 5) are in satisfactory agreement with the experimental data obtained by Chandrasuda and Bradshaw [38]. In the separated shear layer, the shear stress (or C_f) is overpredicted. This implies that in this region, the computed turbulent viscosity is higher than that existing in an actual flow. Results improve somewhat with adaptive refinement of the grid although the scatter in the C_f data precludes any definitive conclusion.

In Fig. 6 the cross stream distribution of the mean u-velocity at different x/S locations is presented. The differences between measurements and predictions should be examined with care since, as stated in Ref. [38] and noted earlier, the hot-wire measurements of the mean velocity

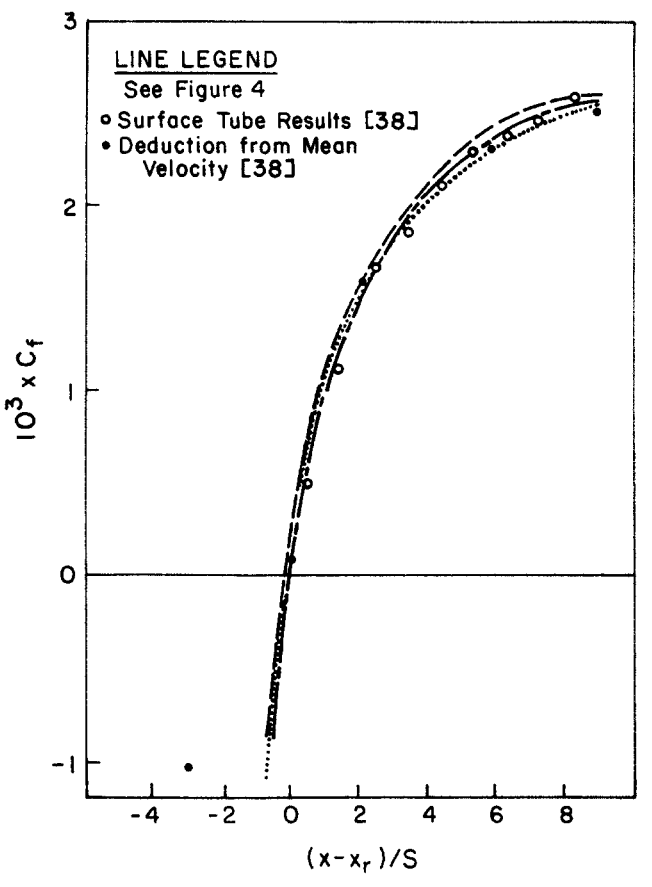


Fig. 5. Skin friction coefficient along the bottom wall of the tunnel (standard turbulence model).

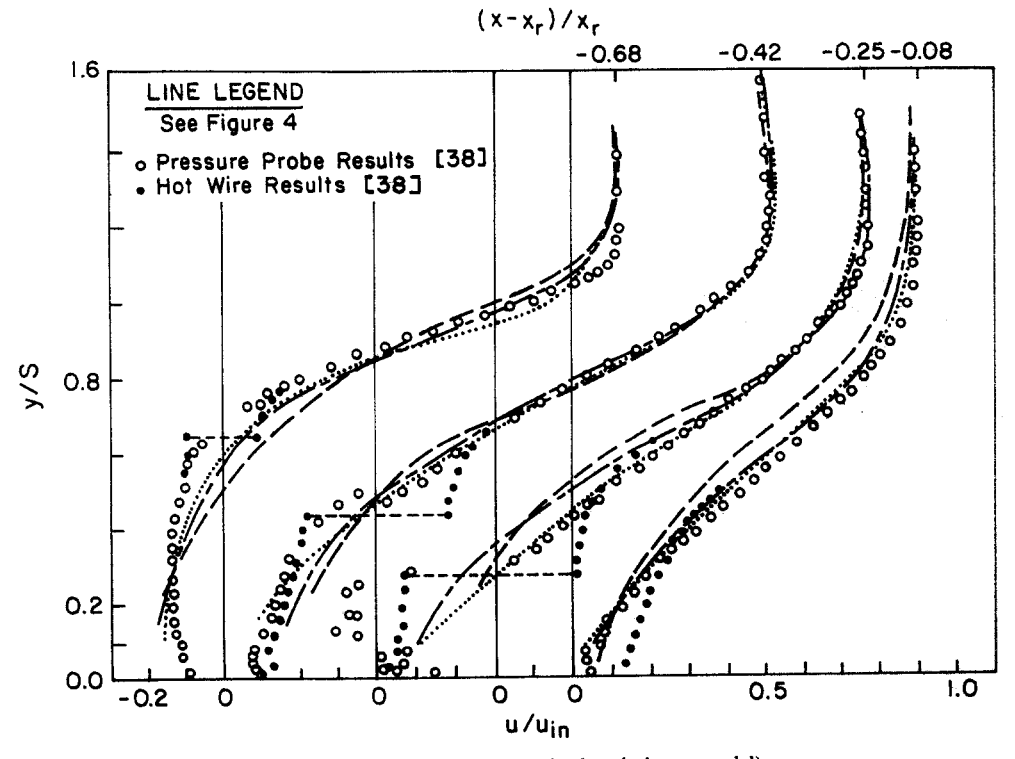


Fig. 6. u-Velocity profiles (standard turbulence model).

profiles inside the recirculation zone are likely to be inaccurate in regions of intermittent separation. In the reverse-flow region or in its vicinity the pressure probe data is probably more reliable. The adaptive grid solution initiated on a 34×16 grid compares well with experimental values and is clearly superior to the 34×16 fixed grid solution. In comparing the 34×16 adaptive grid solution with the same-CPU-effort 50×35 fixed grid calculation, it should be noted that the two solutions are reasonably close to each other at $(x - x_r)/x_r = -0.68$, -0.42 and -0.08, while at $(x - x_r)/x_r = -0.25$ the adaptive grid solution is superior to the same-CPU-effort fixed grid solution. At y/S = 0.4, for example, there is only a 6% difference between the measured values and the 34×16 solution-adapted grid results, but there is a corresponding 58% difference between the measured and the 50×35 fixed grid values.

In Fig. 6, the high velocity gradients across the shear layer can be noticed easily. This causes an increase in the shear stresses and the turbulence kinetic energy and explains the greater concentration of the grid points in this region of the adapted grid (Fig. 3).

The turbulence kinetic energy and dissipation rate at two different locations, one inside the recirculation zone and one downstream of reattachment, are presented in Figs 7 and 8, respectively. The computed values are only in qualitative agreement with experimental data and quantitative agreement is poor. The maximum turbulence intensity rapidly decreases after reattachment. The dissipation rate and kinetic energy predictions in the recirculation region show higher values than those obtained experimentally. This behavior is attributed to the fact that the coefficient c_{μ} used to calculate the turbulent viscosity in the turbulence model is assumed to be constant throughout the computational domain. Improvements in the results are expected if this constant coefficient is replaced by a functional relationship which sensitizes the turbulence model to the effects of streamline curvature, as in the work of Leschziner and Rodi [14]. Moreover, experimental results [38] show that the main feature in the shear stress balances near and downstream of reattachment is a rise in the pressure strain term, which is given by

$$\overline{-(p'/\rho)[(\partial u'/\partial y) + (\partial v'/\partial x)]}.$$
 (39)

Little is known about this term, and it is sometimes neglected for low Mach number flows. However, by sensitizing the turbulence model to the effects of pressure strain interactions including wall damping, Gooray et al. [13] improved the predicted hydrodynamic reattachment length in their study of flow over backward-facing steps. In the present computational effort, the hydrodynamic reattachment length is underpredicted by a distance of more than one step height compared with

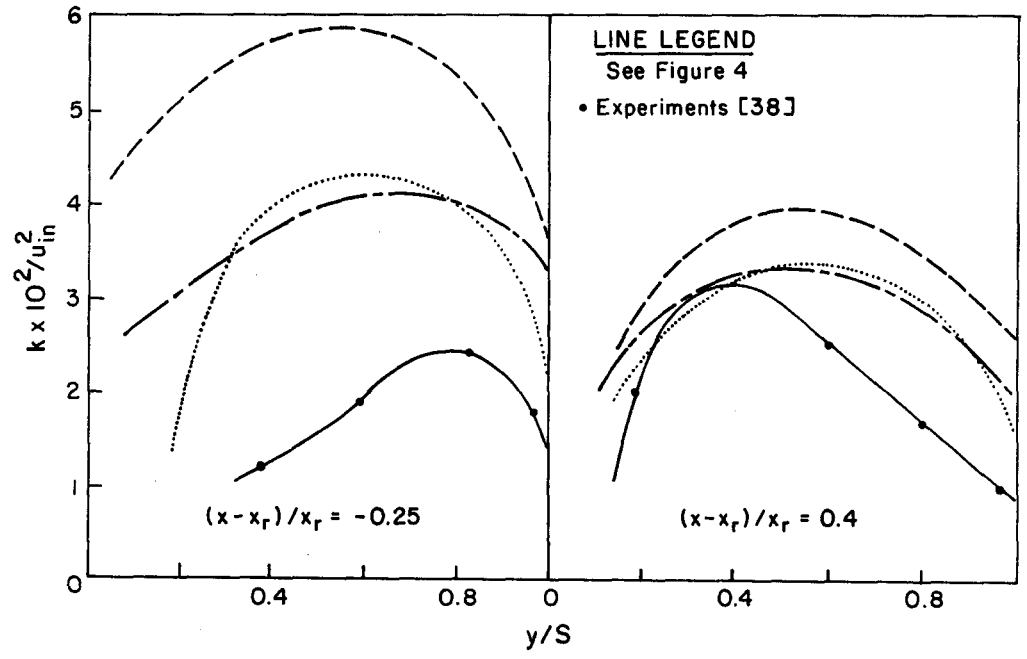


Fig. 7. Turbulence kinetic energy profiles (standard turbulence model).

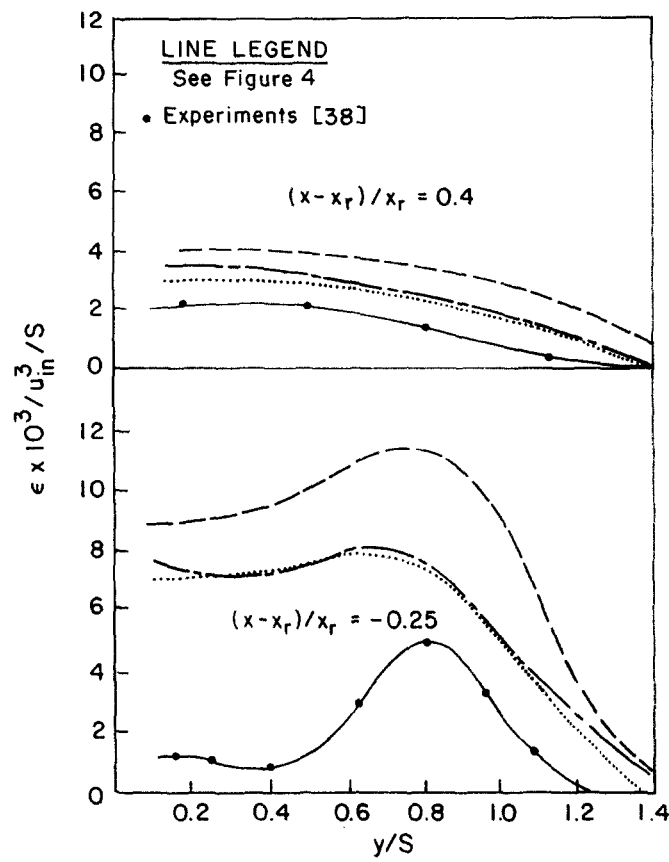


Fig. 8. Turbulence dissipation rate profiles (standard turbulence model).

the experimental value of (6.0 ± 0.5) S. However, the value calculated here is comparable with the numerical predictions reported using a constant c_{μ} value of 0.09 (standard $k-\epsilon$ models underpredict the reattachment length by as much as 20% [40]). This underprediction of the reattachment length is due, as stated earlier, to the higher computed turbulent viscosity in the separated shear layer. Therefore, the modeling error in turbulent separated flows is clearly significant. Nevertheless, numerical error due to high gradients is equally important, as demonstrated in Fig. 7 by the > 50% improvements in the 34 \times 16 grid results obtained after adaptation. In comparing the 34×16 adaptive grid solution with the same-CPU-effort fixed grid solution, the two solutions appear to be comparable, in an overall sense, with each other. The ϵ -profiles (Fig. 8) appear to indicate that the solution-adaptive grid results are somewhat better than the same-CPUeffort fixed grid results. In all the results presented, the differences observed between the predictions employing the same turbulence closure model (i.e. the difference in predictions between the LAME solution-adaptive grid technique and the conventional method) are due to numerical error. As stated earlier, this numerical error is the result of the finite difference representation of partial derivatives (discretization error) or the round-off error. If, in Fig. 7, the differences between the fixed grid solution (---) and the measurements is taken to be the modeling error, this would be inaccurate and any modeling improvements based on this error estimate could be erroneous. The adaptive grid solution reduces the differences between predictions and measurements, and the difference between the adaptive grid solution and the measurements is a better representation of the modeling errors.

The results presented so far have shown the importance of the numerical scheme used to compute turbulent separated flows. It has been shown, through a comparison of the velocity, the turbulent kinetic energy and the dissipation rate profiles, that the solution obtained with the 34×16 adaptive grid method, in the present application, is considerably better than the solution obtained with the conventional method for the same grid size; the adaptive grid solution is either better or comparable with the fixed grid that takes the same level of computational effort.

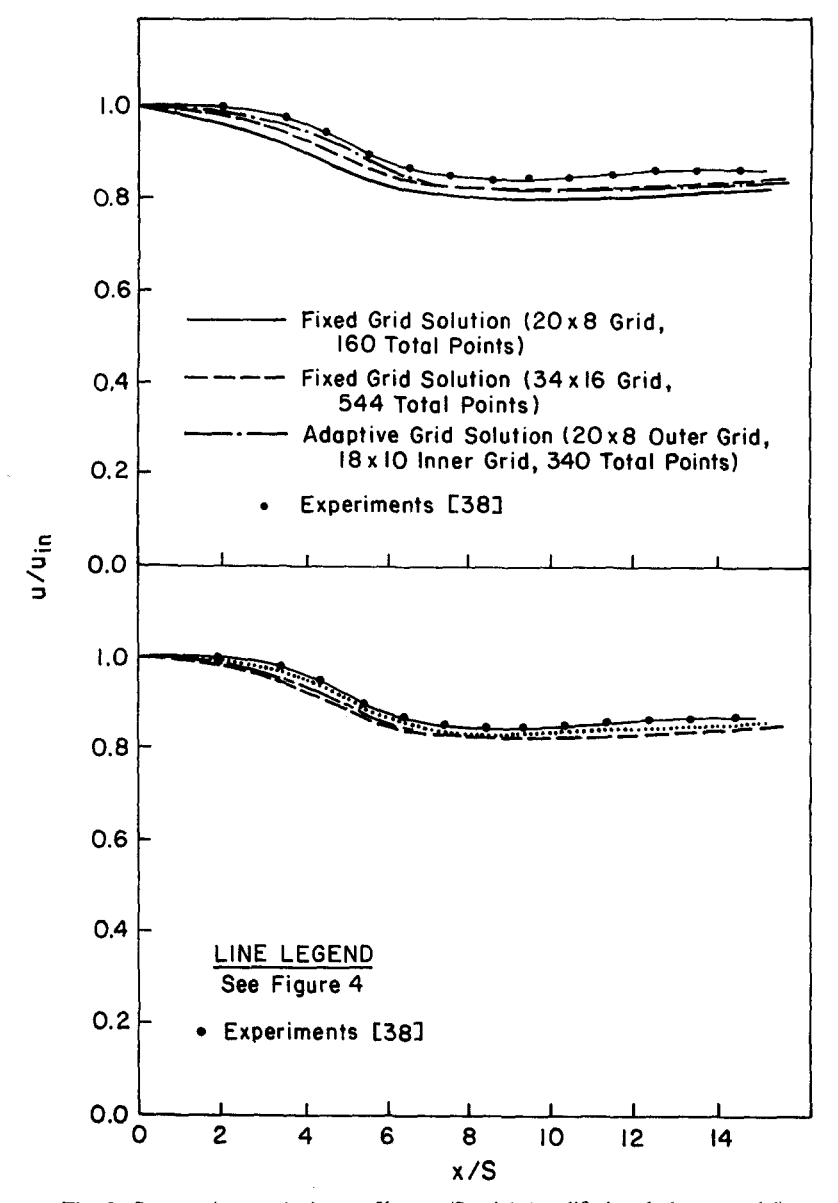


Fig. 9. Streamwise u-velocity profile at y/S = 1.8 (modified turbulence model).

The effect of including the curvature correction is shown in Figs 9-13. As before, results are presented using both the conventional and the adaptive grid method.

The velocity profiles (Figs 9 and 11) show clearly that the solution-adaptive grid is as good as, and in some cases superior to, the same-CPU-effort fixed grid calculation [see the velocity profile in Fig. 11 at $(x - x_r)/x_r = -0.68$ and -0.42]. In all cases the 34 × 16 solution-adaptive grid results are better than the 34 × 16 fixed grid results. At $(x - x_r)/x_r = -0.68$, and y/S = 0.6, for example, the error measure defined as $|(u_{\text{measured}} - u_{\text{predicted}})|/|u_{\text{measured}}|$ is about 0.2 for the solution-adapted grid and about 0.7 for the same-CPU-effort fine grid. At $(x - x_r)/x_r = -0.42$, the error measure at y/s = 0.42, is 0.2 for the solution-adapted grid and 0.62 for the same-CPU-effort fine grid. The corresponding error measure for the same size 34 × 16 fixed grid is several times larger.

Similar observations are also made in the turbulent kinetic energy profiles of Fig. 12 and the dissipation rate profiles of Fig. 13. In Fig. 12, at $(x - x_r)/x_r = 0.4$, and y/S = 0.8, the error measure is 0.27 for the solution-adapted grid and 0.49 for the same-CPU-effort fixed grid. Except for a region near y/s = 0.3, the solution-adapted grid solution is superior. At $(x - x_r)/x_r = -0.25$, the solution-adapted grid is always better. Comparing the solution on the same size grid, the 34 × 16 adapted grid is considerably superior than the 34 × 16 fixed grid. In Fig. 13, at $(x - x_r)/x_r$ of -0.25,

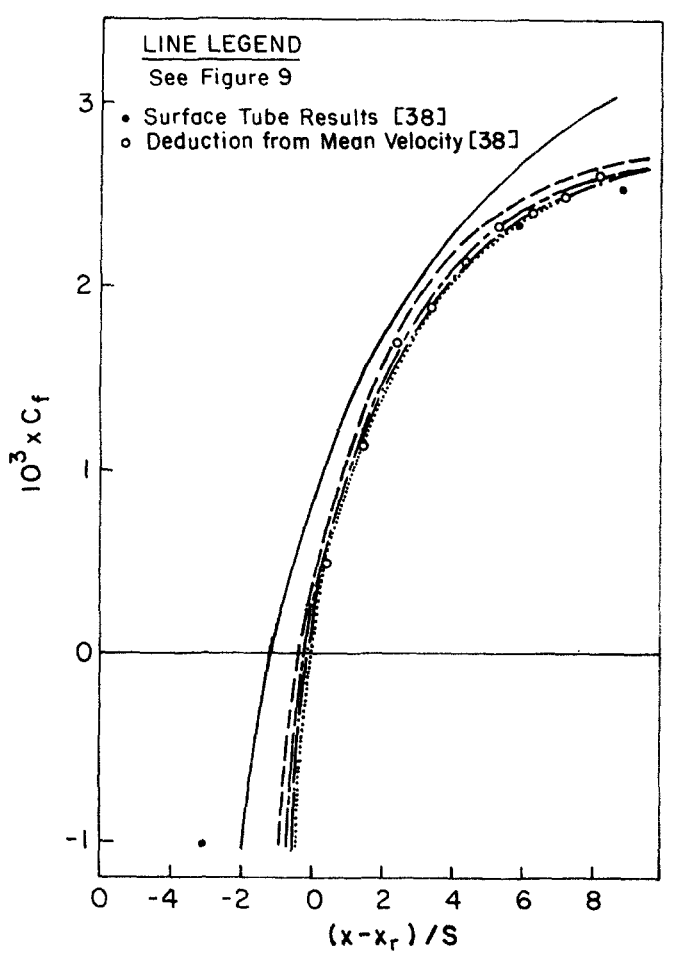


Fig. 10. Skin friction coefficient along the bottom wall of the tunnel (modified turbulence model).

the error measure at y/S = 0.6 is 0.97 for the 50 × 35 fixed grid and 0.67 for the 34 × 16 adapted grid.

The difference between the results presented in Figs 9-13 and those in Figs 4-8 is attributed to the streamline curvature modification (modeling or physical error). As can be seen by comparing both results, curvature effects are very important in correctly predicting turbulent separated flows. The dimension of the recirculation region in this case (6.3S after adaptation) is very close to the experimental value. All results show substantial improvement. The best improvement is obtained with the adaptive grid method which yields results better than those obtained using the same-CPU-effort fixed grid method.

The adaptive grid method is clearly far more accurate than the conventional method, and the difference in the adaptive grid method predictions with and without curvature modification (on a reasonably large mesh) is primarily a physical (modeling) error. The difference in results between the adaptive grid method $(34 \times 16 \text{ grid})$ and the conventional fixed grid method $34 \times 16 \text{ grid}$ is due to the numerical error arising primarily in the high gradient or curvature regions. Therefore, it is possible to better isolate and quantify the physical error due to streamline curvature effects alone (difference between adaptive grid-model predictions with and without curvature effects included) and also the physical error due to the turbulence models used (difference between the adaptive grid solutions and experimental data). To further elaborate, the numerical errors are minimized here through the use of an adaptive grid technique and therefore discrepancies between predictions and measurements can be attributed primarily to turbulence model inaccuracies. This reveals the need for new models which better describe the turbulence process. Clearly, the difference between predictions and measurements in the solution of turbulent flows are not due to physical or numerical errors alone but to a combination of the two, and without

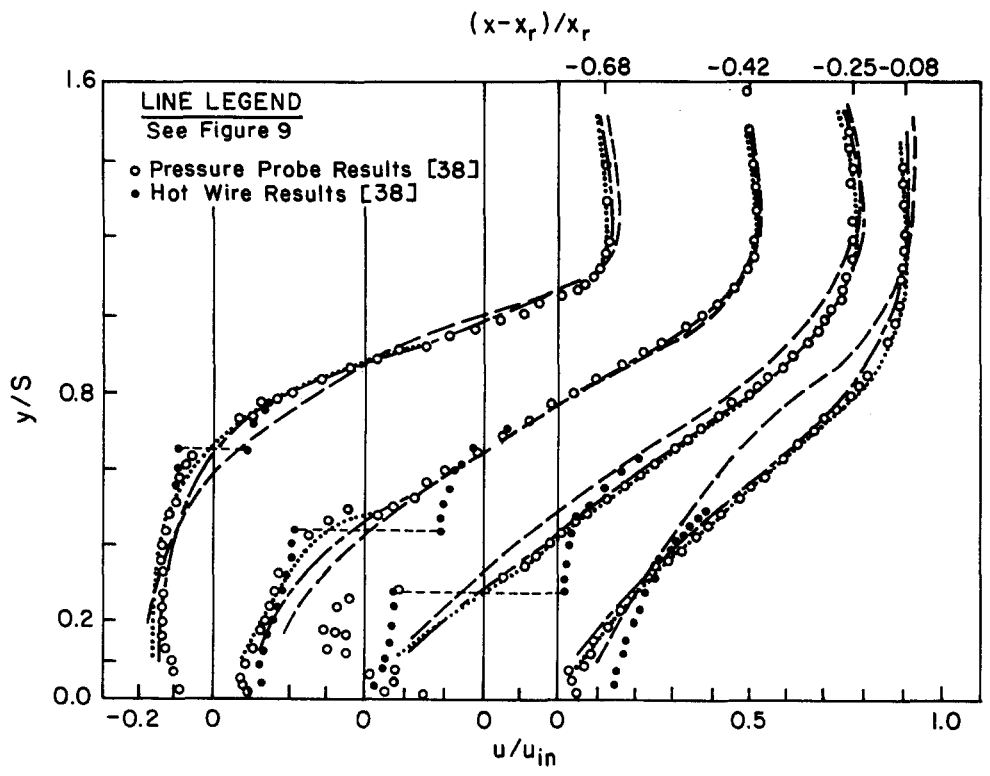


Fig. 11. u-Velocity profiles (modified turbulence model).

proper attention to the selection of a suitably accurate numerical scheme, the numerical errors can be as significant as the modeling errors. It is argued here, that in many cases, with streamline curvature, for example, a same-CPU-effort conventional fixed grid algorithm may not be adequate to reduce numerical errors significantly, and that for a given CPU-effort, using a solution-adaptive grid may be a better way to minimize numerical errors.

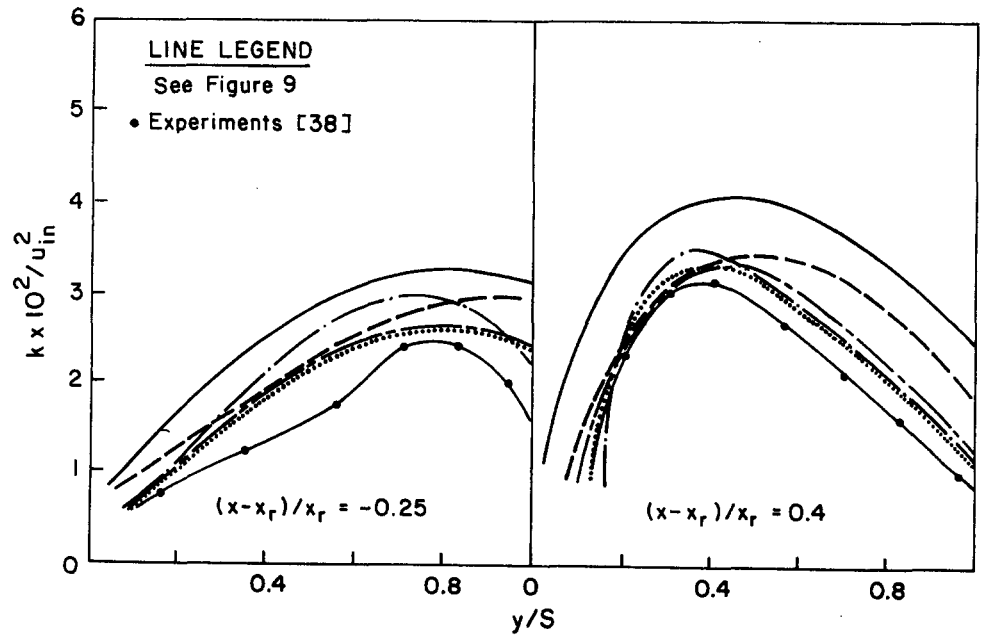


Fig. 12. Turbulence kinetic energy profiles (modified turbulence model).

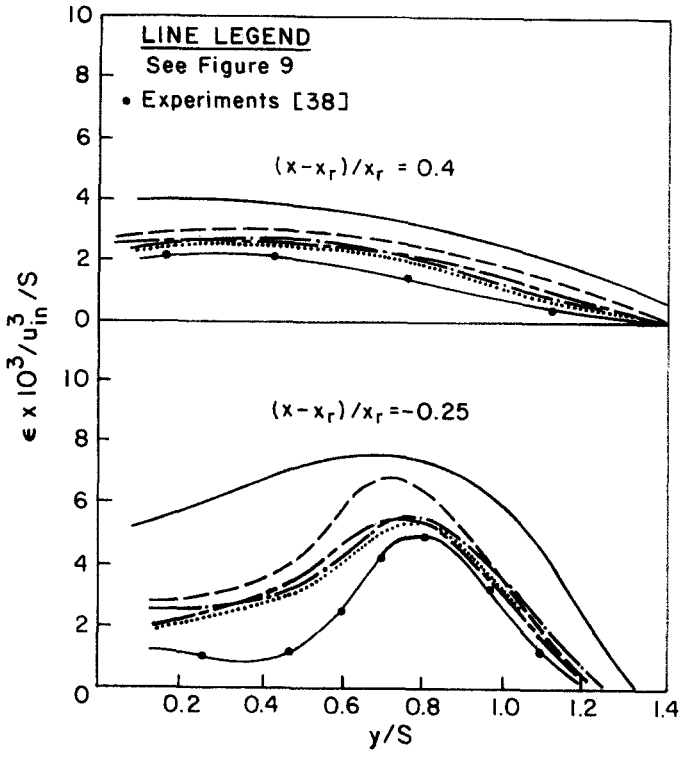


Fig. 13. Turbulence dissipation rate profiles (modified turbulence model).

CONCLUDING REMARKS

An evaluation of the relative importance of the physical and numerical errors associated with the numerical solution of turbulent separated flows, using two turbulence models, with a conventional and a solution-adaptive grid method has been made. The results obtained suggest that adaptive grid methods are more accurate than fixed grid methods for the same level of computational effort. The numerical error is found to be quite large when regions of high gradients are not correctly resolved. Without minimizing numerical errors, no meaningful conclusions concerning the performance of turbulence closure models can be drawn. However, numerical errors in many cases cannot be reduced efficiently without the use of a solution-adaptive grid procedure. The utility of a solution-adaptive grid procedure in reducing numerical errors, and thus providing a better estimate for modeling errors, has been demonstrated for turbulent separated flow over a backward-facing step. The physical error associated with $k-\epsilon$ turbulence models is clearly significant.

REFERENCES

- 1. F. H. Harlow and P. I. Nakayama, Transport of turbulence energy decay rate. Los Alamos Scientific Lab. Report LA-3854, Los Alamos, NM (1968).
- 2. B. E. Launder and D. B. Spalding, Mathematical Models of Turbulence. Academic Press, New York (1972).
- 3. O. K. Kwon and R. H. Pletcher, Prediction of the incompressible flow over a rearward-facing step. Technical Report
- HTL-26, CFD-4, Engng Res. Inst., Iowa State Univ., Ames (1981).
 4. A. M. Gooray, C. B. Watkins and W. Aung, Numerical calculations of turbulent heat transfer downstream of a rearward-facing step. In Proc. 2nd Int. Conf. on Numerical Methods in Laminar and Turbulent Flow, Venice, Italy. Univ. College of Swansea, Wales (1981).
- 5. P. Hutchinson, E. E. Khalil, J. H. Whitelaw and G. Wigley, The calculation of furnace flow properties and their experimental verification. ASME Jl Heat Transfer 81, 276 (1976).
- 6. B. E. Launder, A. P. Morse, W. Rodi and D. B. Spalding, The prediction of free-shear flows: a comparison of the performance of six turbulence models. In Proc. NASA Langley Free Turbulent Shear Flows Conf., Vol. 1. NASA SP 320 (1973).
- 7. W. P. Jones and J. J. McGuirk, Computation of a round turbulent jet discharging into a confined cross flow. In Turbulent Shear Flow 2, pp. 233-245. Springer-Verlag, Heidelberg (1980).
- 8. C. C. Chieng and B. E. Launder, On the calculation of turbulent heat transport downstream from an abrupt pipe expansion. Numer. Heat Transfer 3, 189 (1980).
- 9. W. P. Jones and B. E. Launder, The calculation of low-Reynolds number phenomena with a two-equation model of turbulence. Int. J. Heat Mass Transfer 16, 1119 (1973).

- R. S. Amano, On the calculation of turbulent heat and mass transport downstream from an abrupt pipe expansion. Presented at the AIAA/SAE/ASME 18th Joint Propulsion Conf., AIAA Paper No. 82-1269 (1982).
- A. M. Gooray, C. B. Watkins and W. Aung, k

 ← Calculations of heat transfer in redeveloping turbulent boundary layers downstream of reattachment. Presented at the AIAA/ASME Fluids, Plasma. Thermophysical and Heat Transfer Conf., St Louis, MO. ASME Paper 82-HF-77 (1982).
- A. M. Gooray, C. B. Watkins and W. Aung, Improvements to the k
 multiple model for calculation of turbulent separated forced convection. In Proc. 4th Symp. on Turbulent Shear Flows, Univ. of Karlsruhe, Fed. Rep. Germany (1983).
- 13. A. M. Gooray, C. B. Watkins and W. Aung, A two-pass procedure for the calculation of heat transfer in recirculating turbulent flow. *Numer. Heat Transfer* 6, 423 (1983).
- 14. M. A. Leschziner and W. Rodi, Calculation of annular and twin parallel jets using various discretization schemes and turbulence-model variation. ASME Jl Fluids Engng 103, 352 (1981).
- 15. Y. Nagano and C. Kim, A two-equation model for heat transport in wall turbulent shear flows. ASME Jl Heat Transfer 110, 583 (1988).
- H. A. Dwyer, R. J. Kee and B. R. Sanders, Adaptive grid method for problems in fluid mechanics and heat transfer. AIAA JI 8, 1205 (1980).
- 17. H. A. Dwyer, Grid adaptation for problems in fluid dynamics. AIAA Jl 22, 1705 (1984).
- 18. P. A. Gnoffo, A vectorized finite-volume, adaptive grid algorithm for Navier-Stokes calculations. In *Numerical Grid Generation* (Edited by J. F. Thompson). North-Holland, Amsterdam (1982).
- 19. K. Nakahashi and G. S. Deiwert, A self-adaptive grid method with application to air flow. AIAA Paper No. 85-1525 (1985).
- 20. M. M. Rai and D. A. Anderson, Grid evolution in time asymptotic problems. J. Comput. Phys. 43, 357 (1981).
- 21. P. R. Eisman, Alternating direction adaptive grid generation. AIAA Jl 23, 551 (1985).
- 22. M. J. Berger and A. Jameson, Automatic adaptive grid refinement for the Euler equations. AIAA JI 23, 561 (1985).
- 23. M. C. Thompson and J. H. Ferziger, An adaptive multigrid technique for the incompressible Navier-Stokes equation. J. Comput. Phys. 82, 94 (1989).
- M. J. Berger and J. Oliger, Adaptive mesh refinement for hyperbolic partial differential equations. J. Comput. Phys. 53, 484 (1984).
- S. Acharya and F. H. Moukalled, An adaptive grid solution procedure for convection-diffusion problems. J. Comput. Phys. 91, 32 (1990).
- 26. F. Moukalled and S. Acharya, A local adaptive grid procedure for incompressible flows with multigridding and equidistribution concepts. *Int. J. Numer. Meth. Fluids.* In press.
- S. Acharya and F. H. Moukalled, Improvements to incompressible flow calculation on a non-staggered curvilinear grid. Numer. Heat Transfer 15, 131 (1989).
- 28. S. V. Patankar, Numerical Heat Transfer and Fluid Flow. McGraw-Hill, New York (1980).
- 29. F. H. Hsu, A curvilinear-coordinate method for momentum, heat and mass transfer in domains of irregular geometry. Ph.D. Thesis, Univ. of Minnesota, Minneapolis (1981).
- 30. M. Reggio and R. Camarero, Numerical solution procedure for viscous incompressible flows. *Numer. Heat Transfer* 10, 131 (1986).
- 31. C. M. Rhie and W. L. Chow, Numerical study of the turbulent flow past an airfoil with trainling edge separation. AIAA Jl 21, 1525 (1983).
- 32. S. Abdallah, Numerical solutions for the pressure Poisson equation with Neumann boundary conditions using a non-staggered grid. J. Comput. Phys. 70, 187 (1987).
- 33. F. Moukalled, Adaptive grid solution procedure for elliptic flows. Ph.D. Thesis, Louisiana State Univ., Baton Rouge (1987).
- 34. J. F. Thompson, F. C. Thames and C. W. Martin, Automatic numerical generation of body-fitted curvilinear coordinate system for field containing any number of arbitrary two-dimensional bodies. J. Comput. Phys. 15, 299 (1974)
- 35. D. A. Anderson and J. Steinbrenner, Generating adaptive grids with a conventional grid scheme. Presented at the AIAA 24th Aerospace Science Mtg, Reno, NV (1986).
- 36. B. K., Lee, N. H. Cho and Y. D. Choi, Analysis of periodically fully developed turbulent flow and heat transfer by $k-\epsilon$ equation model in artificially roughened annulus. *Int. J. Heat Mass Transfer* 31, 1797 (1988).
- 37. J. Kim, S. Kline and J. Johnston, Investigation of separation and reattachment of a turbulent shear layer, flow over a backward facing step. Report MD.37, Mech. Engng, Stanford Univ., CA (1978).
- 38. C. Chandrasuda and P. Bradshaw, Turbulence structure of a reattaching mixing layer. J. Fluid Mech. 110, 171 (1981).
- 39. P. Bradshaw and F. Y. F. Wong, The reattachment and relaxation of a turbulent shear layer. J. Fluid Mech. 52, 113 (1972).
- M. Nallaswamy, Turbulence models and their applications to the predictions of internal flows: a review. Computers Fluids 15, 151 (1987).